# The relative roles of the sea surface temperature over the Pacific Meridional Mode and Indian Ocean on tropical cyclone genesis over the North Pacific in super El Niño of 2015

**Takahiro ISHIYAMA**

*Atmosphere and Ocean Research Institute*
*University of Tokyo, Chiba, Japan*

**Masaki SATOH**

*Atmosphere and Ocean Research Institute*
*University of Tokyo, Chiba, Japan*

**Yohei YAMADA**

*Japan Agency for Marine-Earth Science and Technology, Yokohama, Japan*

October 14, 2020
Submitted to Journal of the Meteorological Society of Japan

-----------------------------------

1) Corresponding author: Takahiro Ishiyama, Atmosphere and Ocean Research Institute, The University of Tokyo, 5-1-5, Kashiwanoha, Kashiwa-shi, Chiba 277-8564 JAPAN.
Email: t-ishi@aori.u-tokyo.ac.jp
Tel: +81-04-7136-6051
Fax: +81-04-7136-6056

## Abstract

This study reveals the relative roles of the sea surface temperature (SST) over the Indian Ocean (IO) and the Pacific Meridional Mode (PMM) on tropical cyclone genesis (TCG) in the North Pacific (NP) by focusing on super El Niño event that occurred in 2015. We used the global non-hydrostatic model and conducted perpetual experiments as control for 30 months taking the climatological conditions of July 2015 to examine the sensitivities of SST in the IO and in the region of the PMM to TCG over NP. We showed that if the SST over the PMM region is warmer, the monsoon trough in the western North Pacific (WNP) and vertical wind shear over the Eastern North Pacific (ENP) become weaker, causing reduced TCG in the WNP and increased TCG in the ENP. We also showed that if the SST over the IO is warmer, the monsoon trough in the western North Pacific (WNP) become weaker, although the vertical wind shear over the ENP doesn’t become weaker. We found that with an increase in the SST in the IO or the PMM region, the anticyclonic anomalies over the WNP are intensifying. We confirmed that if the SST is warmer over the PMM region in the absence of the El Niño forcing, the cyclonic anomalies over the WNP is intensifying as in previous studies. Non-linearity was found for the forcing over the PMM region and the El Niño region.

**Keywords:** tropical cyclone; El Niño; Pacific Meridional Mode; monsoon trough; vertical shear

## 1. Introduction

The year 2015 was reported to have experienced the largest El Niño event, while the second largest event occurred in 1997, based on the records from 1950 to 2017 (L'Heureux et al. 2017; Timmermann et al. 2018). During the latter El Niño event, tropical cyclone (hereafter TC) activity over the North Pacific (hereafter NP) was particularly enhanced. Bluden et al. (2016) showed that in 2015, an accumulated cyclone energy was 479 over the Western North Pacific (hereafter WNP) and 288 over the Eastern North Pacific (hereafter ENP), both higher than their respective climatological median values (305 for the WPN and 119 for the EPN). The number of intense TCs was 16 over WNP and 11 over ENP, which were also higher than the climatological median values of 9 and 4, respectively. In addition, the number of named TCs was 26 over the ENP (higher than the climatological median of 17), while the number of TCs over WNP was approximately the same as the climatological median.

In general, El Niño modulates TC activity over the WNP. During the super El Niño years, the frequency of intense TCs increase and the lifetime of TCs become long, and the average position of TC genesis (hereafter TCG) shifts more southeastward (Chan 2000; Wang and Chan 2002; Chan and Liu 2004; Camargo and Sobel 2005; Chen et al. 2006). When super El Niño occurs, monsoon trough, characterized by westerly wind over the WNP near the equator, extends more eastward, leading to an active TC activity over the WNP (Lander 1994; Wu et al. 2012).

Over the ENP, the intensity, frequency, and lifetime of the TCs are increasing, shifting the average position of TCG westwards (Irwin and Davis 1999; Chu 2004; Camargo et al, 2008; Kim et al. 2011; Jin et al. 2014; Fu et al. 2017).

In 2015, in addition to the super El Niño, the sea surface temperature (SST) also increased over the Indian Ocean (hereafter IO) and the region of the Pacific Meridional Mode (hereafter PMM; Chiang and Vimont 2004). When IO is warmer, it is well known that over the WNP, the anticyclones become stronger (Xie et al. 2009) and TCG is suppressed (Zhan et al. 2011; Ha et al. 2015).

During the positive phase of PMM (hereafter PPMM), TCG over both the WNP and the ENP is enhanced owing to the cyclonic anomaly over the WNP and weaker vertical wind shear over the ENP (Zhang et al. 2016; Murakami et al. 2017; Gao et al. 2018).

Previous studies have examined the dependence of TCG over the NP on super El Niño events, IO warming, and PMM. However, the relative roles of the forcings in the three regions (El Niño, IO, and PMM) are not yet clearly understood thus far. Therefore, we focus on the 2015 El Niño event and investigate the influence of the IO warming and PPMM on TCG over the NP.

To examine the relative roles of SST anomalies (hereafter SSTAs), we conducted perpetual sensitivity experiments (Cess and Potter 1988; Iga et al. 2007) by changing the SST patterns in the PMM and the IO using a non-hydrostatic icosahedral atmospheric model (hereafter NICAM; Tomita and Satoh 2004; Satoh et al. 2008, 2014).

This paper is organized as follows: First, in Section 2, the model used in this study is described, together with the experimental settings, method of TC detection, and SST settings. The result of the control experiment taking the climatological conditions of July 2015 is presented in Section 3. Results of the sensitivity experiments are presented in Section 4, discussed in Section 5, and summarized in Section 6.

## 2. Experimental settings and the TC detection method

### *2.1 Model setting*

We use NICAM with the horizontal resolution of 56 km for conducting perpetual experiments in order to determine the sensitivity of TC activity to SST patterns. Grid resolution of 56 km is chosen to reduce computational requirements. However, NICAM might be used at finer horizontal resolution of 14 km. This model also reproduces the multi-scale structure of convection systems with realistic atmospheric circulation (Kodama et al. 2015; Satoh et al. 2017). NICAM with a horizontal resolution of 14 km or less has been used to study the Madden–Julian oscillation and TCs (e.g., Miura et al. 2007; Miyakawa et al. 2014; Nakano et al. 2015; Satoh et al. 2015; Yamada et al. 2017, 2019). It has also been shown that NICAM at coarser resolutions (e.g., 56–220 km) can realistically reproduce the behaviors of convection systems (e.g., their intra-seasonal variability in the tropics) without cumulus parameterization (Yoshizaki et al. 2012; Takasuka et al. 2015, 2018). Based on these studies, numerical experiments in this study were conducted using the 56 km horizontal resolution grid without cumulus parameterization. For the cloud microphysics scheme, we use NICAM single-moment water six-cloud microphysics scheme (NSW6; Tomita 2008); for the planetary boundary layer (PBL) scheme, we use the Mellor Yamada Nakanishi Niino Planetary boundary layer (MYNN scheme; Nakanishi and Niino 2004); for the radiative transfer process mstrnX is used (Sekiguchi and Nakajima 2008); and the minimal advanced treatments of surface interaction and runoff (MATSIRO; Takata et al. 2003) is used for the land surface model.

### *2.2 Perpetual experiment*

A perpetual experiment is an experiment that is conducted without seasonal change. The SST distribution of the control experiment and the solar radiation were fixed for the climatological conditions of July; the conditions were defined by monthly mean of the control SST and solar radiation. Diurnal variations exist for solar radiation. To obtain the initial values of the atmospheric conditions, the Japanese 55-year Reanalysis (hereafter JRA-55; Kobayashi et al. 2015) was used. Simulations were integrated from 00:00 UTC July 1, 2015. In addition, we use the initial value of land pre-adjusted with low resolution NICAM (Kodama et al. 2015). For the SST, the NOAA Optimum Interpolation SST V2 dataset was used. Figure 1 shows the SST patterns (30°E–85°W/60°S–60°N) used in the experiments (control experiment; Fig. 1a) and sensitivity experiments (Figs. 1b,c,d,e,f,g)); the contours represent the values of SST and the colors show the deviation from the climatological values.

We defined three oceanic regions; the El Niño region (160°E–80°W/10°S–10°N), the PMM region (10°N–45°N/110°W–180°W) and the IO region (5°S–30°S/30°E–140°E and 5°S–30°N/30°E–100°E). To examine the SST perturbations in these regions, six sensitivity experiments were conducted. The first experiment is the “Allclm” experiment (Fig. 1b), wherein the SSTA is replaced by climatological SST in all regions; the second is the “PMMclm” experiment (Fig. 1c), in which the SSTA over the PMM region in 2015 is replaced by climatological

SST; the third is the “IOclm” experiment (Fig. 1d), in which SSTA over the IO in 2015 is replaced by climatological SST; in the fourth, PMM + El Niño real experiment (Fig. 1e), we replaced SSTAs by the climatological SST except in the PMM and El Niño regions; in the fifth, El Niño real experiment (Fig. 1f), we replaced SSTAs by the climatological SST except for the El Niño region; and in the sixth PMM real experiment (Fig. 1g), SSTAs are replaced by the climatological SST except for the PMM. Table 1 provides a clear overview of the changes in the SST for the study regions in each sensitivity experiment.

The simulation was conducted for the duration of 46 months; the results of months 16–46 were used for analysis, while the first 15 months were discarded as the spin-up period. For the perpetual experiments representing 30 months, we regarded the results of TCG for each month as one sample, and statistically analyzed TCG results of all 30 samples.

Because the experiment is under the perpetual condition, the land surface temperature is generally warmer than that recorded in the observations. Figure 2 shows the time series of land surface temperature over the selected two domains;

eastern Eurasia (60°E–120°E, 50°N–60°N; black curve) and Indo-Chinese Peninsula (98°E–106°E, 14°N–24°N; blue curve). Eastern Eurasia shows a relatively larger change in surface temperature. Figure 2 shows a continuous increase in temperature from the initial month to approximately 15th month, after which it fluctuates about the quasi-equilibrium state. The bias of the land surface temperature is larger at higher latitudes and moderate in the tropical and sub-tropical regions. Surface temperature near the Indo-Chinese Peninsula, however, shows quasi-equilibrium from the initial month.

In this paper, we show the distribution of TCG in each experiment drawn for 30 months; similarly, the zonal fields of the atmosphere are also averaged for 30 months.

### *2.3 Detection method*

The TC detection method is based on those suggested by Oouchi et al. (2006), Nakano et al. (2015), and Yamada et al. (2017); a TC is identified, provided the following criteria are satisfied for the duration of at least 36 h: (i) the

10 m wind speed is greater than 17.5 m $s^{-1}$, (ii) the sum of a temperature anomaly at 700 hPa, 500 hPa, and 300 hPa is greater than 2 K in a warm core, and (iii) the relative vorticity at 850hPa is greater than $3.5\times10^{-5}$ $s^{-1}$. According to Walsh et al. (2007), a wind speed of 17.5 m $s^{-1}$ is a suitable threshold for TC detection.

*2.4 Observed data and reanalysis data*

To compare the result of control experiment with the observed data, we used the International Best Track Archive for Climate Stewardship (IBTrACS; Knapp et al. 2010) for TC activity and JRA-55 monthly data for atmosphere. As the perpetual experiment represents a statistical equilibrium over the summer season, we used the mean data for July, August, and September (hereafter JAS).

## 3. Results

*3.1 Comparison of the atmospheric circulation*

The results of our experiments well reproduce the characteristics of atmosphere in July 2015. Figure 3 shows the patterns of sea level pressure (hereafter SLP); 850hPa zonal winds of the control experiment taking the climatological conditions of July 2015 are given in Figs. 3a, and 3c), and those of JRA-55 are given in Figs. 3b and 3d.

Figures 3a and 3b show that the strength of the Pacific high of the control experiment is more than that of JRA-55 possibly due to setting of the perpetual July experiment. Figure 2 shows that the surface temperature over the Eurasian Continent of the control experiment is significantly warmer than that for the initial condition. Moreover, the contrast in surface temperature between the Eurasian Continent and the Pacific Ocean is larger in simulations than in observations. This contrast can be reduced if the simulated and observed values of the land surface temperature are brought closer.

However, the differences in the climate values of both data sets show a positive anomaly from the IO to the western part of the WNP and a negative anomaly from the ENP to the region around Japan. These results indicate that the control experiment shows the bias of high pressure anomaly but the differences between the control experiment and Allclm experiment as well as between the climate value and the value of July 2015 in JRA-55 are similar.

Figures 3c and 3d show that in the control experiment, the easterlies along 20°N in the NP are generally stronger than for JRA-55 while the westerlies over the WNP are weaker. However, the region of the westerlies near the equatorial western Pacific, i.e., the monsoon trough, is reproduced at the similar region; from the maritime continent to the dateline. The activity of the monsoon trough is closely related to that of the tropical cyclones in the WNP as previously reported (Lander 1994; Wu et al. 2012; Yamada et al. 2019).

The control experiment is able to reproduce atmospheric circulation only to a certain extent, compared to the 2015 observations or the differences from climate value. Despite these drawbacks, TC activity in the Pacific shows similarities between the experimental and observed values. Thus, we judge that this experiment is useable as the control experiment.

*3.2 TC activity and environmental fields*

Figure 4 shows the geographic distribution of TCG in the control experiment. The number of TCs is larger in the experiment than in the observations, because the experimental duration is 30 times longer than the observational duration (July 2015; one month). The positions of TCG in the experiment are similar to those in the observation, although quantitative comparison is not possible.

Figure 5 shows the boxplot of the number of TCs in each region for the control experiment. The red circles in Fig. 5 are the observed number of TCG points in July 2015. The observed genesis numbers over the NP, WNP and ENP are 8, 3, and 5, respectively, and these are within the simulated probability range presented by the boxes. Specifically, over the NP and the WNP, the observed genesis numbers are within the $25^{th}$ to $75^{th}$ percentile of all samples. The observed genesis number for the ENP is within the top 25 percentiles of all the samples. It should be noted that the observed value need not be close to the median of the sample of the simulation values even if the bias of the model is small. Yamada et al. (2019) conducted 50-member ensemble simulations for the summer seasons of multiple years, including 2015, and showed that the TC number of the ensemble mean of 2015 deviated from the observed value. It is also possible that small horizontal resolution in this simulation might have led to less frequent TCG over the ENP. The horizontal scale of TCs over the ENP is generally smaller than that over other basins (Knaff et al. 2007; Chavas and Emanuel 2010) so the higher resolution is required to realistically reproduce TC activity over the ENP.

We also examined the environmental fields of TCG. Among the components that comprise the Genesis Potential Index (Emanuel and Nolan 2004), we focus on the vertical wind shear and the zonal wind at 850hPa; the latter is related to vorticity.

The strength of the zonal wind at 850hPa in the equatorial WNP indicates the activity of the monsoon trough; in fact, the activity of the monsoon trough is related to TCG in the WNP. Figure 6 shows the relationship between the temporal variability of the monsoon trough and TCG over the WNP by the time–longitude Hovmöller diagrams. The diagram of zonal winds averaged in the latitudinal belt between 0°N and 5°N (which is located to the south of TCG region over the

WNP.) is presented. Figure 6 shows that the westerly winds in the experiment frequently extend eastwards and occasionally progress further towards east beyond the dateline; this occurs when relatively stronger TCs are generated (Chen et al. 2006; Yamada et al. 2019).

Figure 6 also shows that when westerly winds extend eastwards, TCG often occurs over the WNP. This indicates that TCG and the fluctuation of westerly winds correspond well, and TCG often occurs within the monsoon shear line. Previous studies have reported similar results (Ritchie and Holland 1997; Yoshida and Ishikawa 2013). Fluctuation in westerlies also explains variations in the number of TCG over the WNP (Fig.5). Strong westerlies correspond with frequent TCG, whereas weak westerlies are consistent with occasional TCG.

Figure 7 shows vertical wind shear of the control experiment and JRA-55. The latter was calculated using the following equation:

$$\text{Vertical Wind Shear} = \sqrt{(u_{200hPa} - u_{850hPa})^2 + (v_{200hPa} - v_{850hPa})^2} \quad (1)$$

where $u_{200hPa}$ and $u_{850hPa}$ are the zonal winds at 200hPa and 850hPa ($ms^{-1}$), respectively, and $v_{200hPa}$ and $v_{850hPa}$ are the meridional winds at 200hPa and 850hPa ($ms^{-1}$), respectively.

The belt of weak vertical wind shear at 10°N over the ENP is found in both the experiment and JRA-55, thus confirming the reliability of the model experiment.

TCG over the ENP is mostly located in the region of weak vertical wind shear (Fig.4 and Fig.7). TCG over the WNP is also located in this region. These results imply that this belt of weak vertical wind shear may create TCG over the entire NP and indicate that the vertical wind shear has an important role for TCG over NP.

Herein, we showed that the control experiments well reproduce the TCG for 2015. We also found that the environmental fields of 2015 TCG are important for the westerly winds and vertical wind shear over the WNP and the ENP; however, we did not understand the reason for the creation of these environmental fields.

In the following section, we focus on the SST over the PMM region and the IO region, and analyze the relationship between SST and the environmental fields.

## 4. Sensitivity experiments

In this section, we examine how the simultaneous effects of IO warming and PPMM on TC activity under the influence of the super El Niño that occurred in 2015. Table 1 shows the sensitivity experiments in which only SST of the PMM region or the IO region was changed (i.e. PMMclm experiment and IOclm experiment). Sensitivity of each SST region is examined as compared to the control experiment.

Figure 8 shows the distribution of the TCG sites as the number of TCG points counted in boxes of 5° × 5°. Figure 8a shows the distribution in the control experiment, and Figs. 8b and 8c show the difference in distribution between PMMclm and control experiment, and between IOclm and control experiment, respectively.

When comparing the PMMclm and control experiments (Fig. 8b), number of TCG over the WNP increases, while the number of TCG over the ENP decreases. This result indicates that the warmer SST over the PMM region reduces the number of TCG over the WNP, and increasing it over the ENP. Our results on the relationship between TCG over the ENP and SST over the PMM region are consistent with those of Murakami et al. (2017).

Figure 9a shows the SLP of the PMMclm experiment, and the differences in the SLP between the sensitivity experiments and the control experiment (Fig. 3a). Diagonal line areas show where the t-test is 5% significant. The SLP in western part of WNP is higher in the PMMclm experiment than in the control experiment, while the SLP from the eastern part of WNP to the ENP becomes lower than the SLP in the control experiment. This east-west contrast of SLP anomaly is consistent with the difference in TC activity shown in Fig. 8b, and implies that if SST over the PMM region is higher, the environmental fields of TC activity over the western part of the WNP are more unfavorable, while the eastern part of the WNP towards the ENP are more favorable.

In contrast, for the IOclm experiment (Fig. 8c), although the number of TCG over the WNP increases, the number of TCG over the ENP does not show a significant difference. This indicates that the warmer SST over the IO has an impact on decreasing the number of TCG over the WNP; however, the number of TCG over the ENP is not radically changed by the warmer SST over the IO region.

Figure 9b is similar to 9a, but for the results of the IO experiment. This sensitivity experiment shows that the SLP in western parts of the WNP becomes higher than the SLP in the control experiment. However, in the ENP, no such differences in the SLP exist. This result is consistent with the difference in TC activity and indicates that the warmer IO only has an impact on the TC activity over the WNP.

Figures 10a and 10b show zonal winds at 850hPa and positions of TC genesis for PMMclm and IOclm experiments. Figures 10c and 10d show the difference in zonal winds from these two sensitivity experiments from those of the control experiment. Diagonal line areas show where the t-test is 5% significant.

Figure 10c shows that westerly winds become stronger in the equatorial WNP from the Philippines towards the dateline (Figs. 10a and 10b) compared to those of the control experiment (Fig. 3c). Figure 10d also shows similar magnitude of the difference in westerly winds in the equatorial WNP, but it does not show any impact on the ENP.

We consider that the increase in the number of TCG over the WNP (Fig. 8) is due to the intensification of westerly winds. In addition, Figs. 12a and 12b show that TC genesis mainly occurs in the region of the wind shear line between the westerly and the easterly winds over the WNP. Therefore, warmer SST over the PMM region and the IO weakens the westerly winds corresponding to the monsoon trough, and as a result, TCG over the WNP decreases.

Figures 11a and 11b show the average vertical wind shear of PMMclm and IOclm experiments, and Figs. 11c and 11d show the differences in vertical wind shear between the control experiment and the two sensitivity experiments. Diagonal line areas show where the t-test is 5% significant. Figure 11c shows stronger shear in the PMMclm simulation for the ENP. In contrast, Fig. 11d shows that the vertical shear over the ENP does not have notable variability.

The decrease in the number of TCG over the ENP (Fig. 8) is due to the intensification of vertical wind shear. This result indicates that in the ENP, warmer SST over the PMM region weakens the vertical wind shear and TCG increases, while warmer SST over the IO region has no impact on TC.

Figures 11c and 11d also show that when the SST over the PMM region and the IO region is warmer, the vertical wind shear over the WNP is stronger. However, as shown in Figs. 8b and 8c, the number of TCG in each sensitivity experiment is higher than that in the control experiment, which is inconsistent with the results in Figs. 11c and 11d. Therefore, we conclude that the influence of the SST over the PMM and the IO regions on TCG over the WNP in 2015 can be attributed more due to the westerly wind modulation than to the vertical wind shear modulation.

In this section, we showed that when the SST over the PMM region and the IO region is warmer under strong 2015 El Niño, the westerly winds over the WNP are weaker, reducing the number of TCG over the WNP. When vertical wind shear over the ENP is weaker, the number of TCG in the ENP increases. Our results are similar to those reported in previous studies (i.e. Zhan et al. 2011; Ha et al. 2015; Murakami et al. 2017) with respect to the influence of IO warming on TC activity over the WNP, and of the PPMM on TC activity over the ENP. However, our results differ from those shown in previous studies regarding the influence of PPMM on TC activity over the WNP (Zhang et al. 2016; Zhan et al. 2017; Hong et al. 2018; Wu et al. 2018; Gao et al. 2018). These indicate that positive SSTAs over the PMM regions cause a cyclonic response over the WNP, and that these anomalies provide favorable conditions for TC activity over the WNP. The relationship between the PPMM and the environmental fields of TC activity over the WNP are discussed in the next section.

## 5. **The influence of the PPMM on TCG over the WNP in 2015**

To examine the relationship between the PPMM and the environmental fields of TCG, we conducted additional sensitivity experiments using the SST (Figs.

1b,e,f,g). Figures 12a, 12b and 12c show the differences in the of zonal wind field at 850hPa between the control and the PMMclm experiments, the El Niño + PMM real and the El Niño real experiments, and the PMM real and Allclm experiments, respectively. Figure 12a shows the difference in the presence or absence of the PPMM in the SST of 2015. Figure 12b shows the difference in the presence or absence of the PPMM in the SST of only super El Niño in 2015, and Fig. 12c shows the difference in the presence or absence of the PPMM under the condition of no difference in other basins including the El Niño region. In particular, the difference shown in Fig. 12c follows previous studies.

Figure 12a shows an anomalous cyclonic circulation over the ENP and an anomalous anticyclonic circulation over the WNP. The latter causes the weakening of the monsoon trough (Fig. 10c). Figure 12b also shows the same anomalous circulation as that in Fig. 12a over the WNP and the ENP. Such anomalous circulation might be explained by the presence/absence of the PPMM under El Niño 2015 event, and co-existence of the PPMM and super El Niño which together lead to unfavorable environmental fields for TCG over the WNP.

Figure 12c shows the anomalous cyclonic circulation over the WNP; this is similar to the results reported in previous studies, and indicates that the environmental fields of TCG are favorable under the PPMM. Result shown in Fig. 12c is the reverse of the results shown in Figs. 12a and 12b.

Our results indicate that the circulation response over the WNP to the SSTA in the PMM region depends on the phase of El Niño-Southern Oscillation (ENSO). Positive PMM induces the anticyclonic response over the WNP during El Niño events, while it induces the cyclonic response over the WNP in the absence of El Niño. This implies that the response to the SSTAs over the PMM and El Niño regions is not additive, which might explain the difference between our results and those from the previous studies; our research shows the role of the PPMM and El Niño on TCG over the WNP while previous studies have focused on the relationship between TCG and the PPMM.

## 6. Summary and Conclusions

The aim of this study was to reveal the influence of the IO warming and the PPMM on TCG over the NP during the super El Niño event in 2015. In this study, perpetual July experiments were conducted for 30 months using NICAM. It was confirmed that the control experiment taking the climatological conditions of July 2015 successfully reproduced TCG and environmental fields including the monsoon trough with zonal winds over the equatorial and sub-tropical NP.

We also investigated the impact of SSTAs in the PMM and the IO regions during the super El Niño in 2015. For this purpose, we conducted PMMclm and IOclm experiments and compared them with control experiment. We found that both the PMMclm and IOclm experiments show lower SLP and stronger westerly winds over the WNP compared to the control experiment. This indicates that SST warming in the two regions has negative effects on TCG over the WNP. In addition, the IOclm experiment shows that warming over the IO is not responsible for anomalous vertical wind shear, and has little influence on TCG over the ENP compared to the control experiment.

To examine the role of PPMM on TCG over the WNP in 2015, we conducted additional experiments. We found that under super El Niño, the difference in presence (or absence) of the PPMM causes the environmental fields of TCG to become unfavorable (or favorable). This result has not been reported in previous studies, and can add to the existing literature.

The present study confirmed variability in TCG caused by the atmospheric internal modes. The number of TCs shows large variance under the same SST condition. Moreover, TC activities are not only dependent on the environmental conditions (such as SST distribution), but also are a function of variability related to fluctuations (such as intra-seasonal variability, under the same environmental conditions). This effect should be taken into consideration to better understand the relationship between TC activities and SST patterns for improved seasonal forecasting.

The effects of atmosphere-ocean interactions were not considered in this study. It is known that the interactions between the atmosphere and the ocean affect TC activities. Moreover, the effect of TCs on the cooling of SST through oceanic upwelling is significant. For example, Schade and Emanuel (1999) studied the differences in TC development using atmospheric and coupled atmosphere–ocean models. They showed that based on the atmospheric model, the pressure of the typhoon was approximately 30 hPa higher when compared to the coupled atmosphere–ocean model. Moreover, Lin et al. (2008) showed that local subsurface ocean warming induces strong typhoons. To consider the interactions between the large-scale atmospheric circulation and the SST distribution at the seasonal scale, future research will incorporate a high-resolution coupled atmosphere–ocean model (e.g. Miyakawa et al. 2017), to analyze the relationship between atmosphere-ocean interaction and TCs.

## Declaration

The authors have no conflicts of interest to declare.

## Author contributions

T.I. and M.S.designed this study. T.I. executed this study and wrote the manuscript. M.S. and Y.Y. edited and approved the manuscript.

## Data Availability Statement

The numerical experimental data are provided by requests to the authors.


## Acknowledgments

In this study, we used the Japanese 55-year Reanalysis (JRA-55) data. We also used the Grads software to plot the results and Oakleaf-FX10 of the Information Technology Center of the University of Tokyo to conduct all numerical experiments. This work is supported by the FLAGSHIP2020, MEXT within the priority study (No.4: Advancement of meteorological and global environmental predictions utilizing observational “Big Data”).


## References

Bluden, J., and D. S. Arndt, Eds., 2016: State of the Climate in 2015. Bull. Amer. Meteor. Soc., 97 (8), S1-S275, DOI:10.1175/2016BAMSStateoftheClimate.1

Camargo, S. J., and A. H. Sobel, 2005: Western North Pacific tropical cyclone intensity and ENSO. J. Climate, **18**, 2996–3006, doi:10.1175/ JCLI3457.1.

Camargo, S. J., M. C. Wheeler and A. H. Sobel, 2009: Diagnosis of the tropical cyclogenesis using an empirical index. JAS, 75, 3061-3074, doi:10.1175/2009JAS3101.1.

Cess, R. D., and J. B. Klemp, 1988: A methodology for understanding and intercomparing atmospheric climate feedback processes in general circulation models. J. Geophys. Res., **93**, 8305-8314. doi:10.1029/JD093iD07p08305.

Chan, J. C. L., 2000: Tropical cyclone Activity over the western north Pacific associated with El Niño and La Niña events. J. Climate, **13**, 2960-2972, doi:10.1175/1520-0442(2000)013<2960:TCAOTW>2.0.CO;2.

Chan. J. C. L., and K. S. Liu, 2004: Global warming and western north Pacific typhoon activity from an observational perspective. J. Climate, **17**, 4590-4602, doi:10.1175/3240.1.

Chavas, D. R., and K. A. Emanuel, 2010: A QuikSCAT climatology of tropical cyclone size. Geophys. Res. Lett, 37, L18816, doi:10.1029/2010GL044558.

Chen, T. C., S. Y. Wang, and M. C. Yen, 2006: Interannual variation of tropical cyclone activity over the western North Pacific. J. Climate, **19**, 5709–5720, doi:10.1175/JCLI3934.1.

Chiang, J. C. H., and D. J. Vimont, 2004: Analogous Pacific and Atlantic meridional modes of tropical atmosphere–ocean variability. J. Climate, **17**, 4143–4158, doi:10.1175/JCLI4953.1.

Emanuel, K. A., and D. S. Nolan, 2004: Tropical cyclone activity and global climate. Preprints, 26$^{th}$ Conf. on Hurricanes and Tropical Meteorology, Miami, FL, Amer. Meteor. Soc., 240–241.

Gao, S., L. Zhu, W. Zhang, and Z. Chen, 2018: Strong modulation of the Pacific meridional mode on the occurrence of intense tropical cyclones over the western north Pacific. J. Climate, **31**, 7739-7749, doi:10.1175/JCLI-D-17-0833.1.

Ha, Y., Z. Zhong, X. Yang and Y. Sun, 2015: Contribution of east Indian Ocean SSTA to western north Pacific tropical cyclone activity under El Niño/La Niña conditions. Int. J. Climatol, **35**, 506-519, doi: 10.1002/joc.3997

Hong, C. –C., and M. –Y. Lee, H. –H. Hsu, and W. –L. Tseng, 2018: Distinct influences of the ENSO-like and PMM-like SST anomalies on the mean TC genesis location in the western north Pacific: the 2015 summer as an extreme example. J. Climate., **31**, 3049-3059, doi:10.1175/JCLI-D-17-0504.1.

Iga, S., H. Tomita, Y. Tsushima, and M. Satoh, 2007: Climatology of a nonhydrostatic global model with explicit cloud processes. Geophys. Res. Lett., **34**, L22814, doi:10.1029/2007GL031048.

Knaff, J. A., C. R. Sampson, M. Demaria, T. P. Marchok, J. M. Gross, and C J. Mcadie, 2007: Statistical tropical cyclone wind radii prediction using climatology and persistence. Wea. Forcasting, **22**, 781-791, doi:10.1175/WAF1026.1.

Knapp, K. R., M. C. Kruk, D. H. Levinson, H. J. Diamond, and C. J. Neumann, 2010: The International Best Track Archive for Climate Stewardship (IBTrACS). Bull. Amer. Meteor. Soc., **91**, 363–376, doi:10.1175/2009BAMS2755.1.

Kobayashi, S., Y. Ota, Y. Harada, A. Ebita, M. Moriya, H. Onoda, K. Onogi, H. Kamahori, C. Kobayashi, H. Endo, K. Miyaoka, and K. Takahashi, 2015: The JRA-55 Reanalysis: General specifications and basic characteristics. J. Meteor. Soc. Japan, **93**, 5-48, doi:10.2151/jmsj.2015-001.

Kodama, C., Y. Yamada, A. T. Noda, K. Kikuchi, Y. Kajikawa, T. Nasuno, T. Tomita, T. Yamaura, T. G. Takahashi, M. Hara, Y. Kawatani, M. Satoh, and M. Sugi, 2015: A 20-year climatology of a NICAM AMIP-type simulation. J. Meteor. Soc. Japan, **93**, 393-424, doi:10.2151/jmsj.2015-024

Lander, M. A., 1994: An exploratory analysis of the relationship between tropical strom formation in the western north Pacific and ENSO, Mon. Wea. Rev., **122**, 636-651, doi:10.1175/1520-0493(1994)122<0636:AEAOTR>2.0.CO;2.

L'Heureux M. L., K. Takahashi, A. B. Watkins, A. G. Barnston, E. J. Becker, T. E. T. E. Di Liberto, F. Gamble, J. Gottschalck, M. S. Halpert, B. Huang, K.

Mosquera-Vásquez, and A. T. Wittenberg, 2016: Observing and predicting the 2015-16 El Niño. Bull Amer. Meteor. Soc., **98**, 1363-1382, doi:10.1175/BAMS-D-16-0009.1.

Lin, I. I., C. C. Wu and I. F. Pun, 2008: Upper-ocean thermal structure and the western North Pacific category 5 typhoons. Part I: ocean Features and the category 5 typhoons' Intensification. Mon. Wea. Rev., **136**, 3288-3306, doi:10.1175/2008MWR2277.1.

Oouchi, K., J. Yoshimura, H. Yoshimura, R. Mizuta, S. Kusunoki, and A. Noda, 2006: Tropical cyclone climatology in a global warming climate as simulated in a 20 km mesh global atmospheric model: Frequency and intensity analysis. J. Meteor. Soc. Japan, **84**, 259-276, doi:10.2151/jmsj.84.259

Miura, H., M. Satoh, T. Nasuno, A. T. Noda and K. Oouchi, 2007: A Madden-Julian Oscillation event simulated using a global cloud-resolving model. Science, **318**, 1763-1765. doi:10.1126/science.1148443

Miyakawa, T., M. Satoh, H. Miura, H., Yashiro, A. T. Noda, Y. Yamada, C. Kodama, M. Kimoto and K. Yoneyama, 2014: Madden-Julian Oscillation prediction skill of a new-generation global model. Nature Commun., **5**, 3769. doi:10.1038/ncomms4769.

Miyakawa, T., H. Yashiro, T. Suzuki, H. Tatebe and M. Satoh, 2017: A Madden-Julian Oscillation event remotely accelerates ocean upwelling to abruptly terminate the 1997/1998 super El Niño. Geophys. Res. Lett., DOI:10.1002/2017GL074683

Murakami, H., G. A. Vecchi, T. L. Delworth, A. T. Wittenberg, S. Underwood, R. Gudgel, X. Yang, L. Jia, F. Zeng, K. Paffendorf and W. Zhang, 2017: Dominat role of subtropical Pacific warming in extreme eastern Pacific seasons: 2015 and future. J. Climate, **30**, 243-264, doi:10.1175/JCLI-D-16-0424.1.

Nakanishi, M. and H. Niino, 2004: An improved Mellor-Yamada Level-3 model with condensation physics: It's design and verification. Bound.-Layer Meteor., **112**, 1-31. doi:10.1023/B:BOUN.0000020164.04146.98.

Nakano, M., M. Sawada, T. Nasuno, and M. Satoh, 2015: Intraseasonal variability and tropical cyclogenesis in the western North Pacific simulated by a global nonhydrostatic atmospheric model. Geophys. Res. Lett., **42**, 565-571, doi:10.1002/2014GL062479.

Ritchie, E. A., and G. J. Holland, 1999: Large-scale patterns associated with tropical cyclogenesis in the western Pacific. Mon. Wea. Rev., **127**, 2027-2043, doi:10.1175/1520-0493(1999)127<2027:LSPAWT>2.0.CO;2

Satoh, M., T. Matsuno, H. Tomita, H. Miura, T. Nasuno, and S. Iga, 2008: Nonhydrostatic icosahedral atmospheric model (NICAM) for global cloud resolving simulations. J. Comput. Phys., **227**, 3486–3514, doi: 10.1016/j.jcp.2007.02.006

Satoh, M., H. Tomita, H. Yashiro, H. Miura, C. Kodama, T. Seiki, A. T. Noda, Y. Yamada, D. Goto, M. Sawada, T. Miyoshi, Y. Niwa, M. Hara, T. Ohno, S. Iga, T. Arakawa, T. Inoue and H. Kubokawa, 2014: The non-hydrostatic icosahedral atmospheric model: description and development. Prog. in Earth and Planet. Sci. **1**: 18, doi: 10.1186/s40645-014-0018-1.

Satoh, M., Y. Yamada, M. Sugi, C. Kodama and A. T. Noda, 2015: Constraint on future change in global frequency of tropical cyclones due to global warming. J. Meteorol. Soc. Japan, **93**, 489-500, doi:10.2151/jmsj.2015-025.

Satoh, M., H. Tomita, H. Yashiro, Y. Kajikawa, Y. Miyamoto, T. Yamaura, T. Miyakawa, M. Nakano, C. Kodama, A. T. Noda, T. Nasuno, Y. Yamada and Y. Fukutomi, 2017: Outcomes and challenges of global high-resolution non-hydrostatic atmospheric simulations using the K computer. Progress in Earth and Planetary Science, 4, 13, doi:10.1186/s40645-017-0127-8.

Schade, L. R., and K. A. Emanuel, 1999: The ocean’s effect on the intensity of tropical cyclones: results from a simple coupled atmosphere-ocean model. J. Atmos. Sci., **56**, 642-651, doi: 10.1175/1520-0469(1999)056<0642:TOSEOT>2.0.CO;2.

Sekiguchi, M. and T. Nakajima, 2008: A k-distribution-based radiation code and its computational optimization for an atmospheric general circulation model. J. Quant. Spectrosc. Radiat. Transfer., **109**, 2779-2793, doi:10.1016/j.jqsrt.2008.07.013

Takasuka, D., T. Miyakawa, M. Satoh, H. Miura, 2015: Topographical effects on the internally produced MJO-like disturbances in an aqua-planet version of NICAM. SOLA, **11**, 170-176, doi:10.2151/sola.2015-038

Takasuka, D., M. Satoh, T. Miyakawa and H. Miura, 2018: Initiation Processes of the Tropical Intraseasonal Variability Simulated in an Aqua-planet Experiment: What is the Intrinsic Mechanism for MJO Onset? J. Adv. Model. Earth Syst., accepted.

Takata, K., S. Emori, and T. Watanabe, 2003: Development of the minimal advanced treatments of surface interaction and runoff. Global. Planet. Change, **38**, 209–222, doi: 10.1016/S0921-8181(03)00030-4

Timmermann, A., S. –I. An, J. –S. Kug, F. –F. Jin, W. Cai, A. Capotondi, K. Cobb. M. Lengaigne, M. J. McPhaden, M. F. Stuecker, K. Stein, A. T. Wittenberg, K. –S. Yun, T. Bayr, H. –C. Chen, Y. Chikamoto, B. Dewitte, Di. Dommenget, P. Grothe, E. Guilyardi, Y. –G. Ham, M. Hayashi, S. Ineson, D. Kang, S. Kim, W. Kim, A. Santoso, K. Takahashi, A. Todd, G. Wang, G. Wang, R. Xie, W. –H.

Yang, S. –W. Yeh, J. Yoon, E. Zeller, and X. Zhang, 2018: El Niño-Southern oscillation complexity. Nature, **559**, 535-545, doi:10.1038/s41586-018-0252-6.

Tomita, H., and M. Satoh, 2004: A new dynamical framework of nonhydrostatic global model using the icosahedral grid. Fluid Dyn. Res., **34**, 357–400, doi:10.1016/j.fluiddyn.2004.03.003

Tomita, H., 2008: New microphysical schemes with five and six categories by diagnostic generation of cloud ice. J. Meteor. Soc. Japan, **86A**, 121–142, doi: 10.2151/jmsj.86A.121

Walsh, K., M. Fiorino, C. W. Landsea, and K. L. McInnes, 2007: Obsjectively determined resolution-dependent threshold criteria for the detection of tropical cyclones in climate models and reanalyses. J. Climate, **20**, 2307-2314, doi:10.1175/JCLI4074.1.

Wang, B., and J. C. L. Chan, 2002: How strong ENSO events affect tropical storm activity over the western North Pacific. J. Climate, **15**, 1643–1658, doi:10.1175/1520-0442(2002)015,1643: HSEEAT.2.0.CO;2.

Wu, L., Z. Wen, R. Huang, and R. Wu, 2012: Possible linkage between the monsoon trough variability and the tropical cyclone activity over the western North Pacific. Mon. Wea. Rev., **140**, 140–150, doi:10.1175/MWR-D-11-00078.1.

Wu, Y. K., C. –C. Hong, and C. –T. Chen, 2018: Distict effects of the two strong El Niño events in 2015-2016 and 1997-1998 on the western north Pacific monsoon and tropical cyclone activity: role of subtropical eastern north Pacific warm SSTA. J. Geophys. Res., **123**, doi:10.1002/2018JC013798.

Xie, S.-P., K. Hu, J. Hafner, H. Tokinaga, Y. Du, G. Huang, and T. Sampe, 2009: Indian Ocean capacitor effect on Indo– western Pacific climate during the summer following El Niño. J. Climate, **22**, 730–747, doi:10.1175/2008JCLI2544.1.

Yamada, Y., M. Satoh, M. Sugi, C. Kodama, A. T. Noda, M. Nakano and T. Nasuno, 2017: Response of tropical cyclone activity and structure to global warming in a high-resolution global nonhydrostatic model. J. Clim., **30**, 9703-9724, doi:10.1175/JCLI-D-17-0068.1.

Yamada, Y., C. Kodama, M. Satoh, M. Nakano, T. Nasuno, and M. Sugi, 2019: High-resolution ensemble simulations of intense tropical cyclones and their internal variability during the El Ninos of 1997 and 2015. Geophys. Res. Lett., **46**, 7592-7601, doi:10.1029/2019GL082086.

Yoshida, R., and H. Ishikawa, 2013: Environmental factors contributing to tropical cyclone genesis over the western north Pacific. Mon. Wea. Rev., **141**, 451-467, doi:10.1175/MWR-D-11-00309.1.

Yoshizaki, M., S. Iga and M. Satoh, 2012: Eastward-propagating property of large-scale precipitation systems simulated in the coarse-resolution NICAM and an explanation of its formation. SOLA, **8**, 21-24. doi:10.2151/sola.2012-006

Zhan, R., Y. Wang, and C. C. Wu, 2011: Impact of SSTA in the East Indian Ocean on the frequency of northwest Pacific tropical cyclones: A regional atmospheric model. J. Climate, **24**, 6227–6242, doi:10.1175/JCLI-D-10-05014.1.

Zhan, R., Y. Wang and Q. Liu, 2017: Salient differences in tropical cyclone activity over the western North Pacific between 1998 and 2016. J. Climate, **30**, 9979-9997, doi:10.1175/JCLI-D-17-0263.1.

Zhang, W., G. A. Vecchi, H. Murakami, G. Villarini, and L. Jia, 2016: The Pacific meridional mode and the occurrence of tropical cyclones in the western North Pacific. J. Climate, **29**, 381–398, doi:10.1175/JCLI-D-15-0282.1.

## List of Figures

Fig. 1 SST distributions of (a) the 2015 experiment, (b) the Allclm experiment, (c) the PMMclm experiment, (d) the INDclm experiment, (e) the PMM + El Niño experiment, (f) the El Niño experiment and (g) the PMMreal experiment. Only SSTs in the region (30°E–85°W/60°S–60°N) are shown. The contours denote the values of SST in July 2015 and the shades are the differences between experiments and the climate value (1982–2011, July average). Bold lines show that SST is 300K. Solid lines of low latitude side are drawn every 1K, while solid lines of high latitude side are drawn 3K.

Fig. 2 Time series (moving average of anteroposterior 2 weeks) of the domain mean surface temperature for 46 months in the 2015 experiment. The black line denotes Eurasian continent (60°E–120°E/50°N–60°N), the blue line denotes Indochinese Peninsula (98°E–106°E/14°N–24°N).

Fig. 3 Average SLPs over the 30 months of (a) the 2015 experiment. (b) Same as (a) but for the SLP of JRA-55; (b) JAS 2015. The contour in Figs. 3a and 3b denotes the each SLP, respectively. The shade denotes the difference between the value of simulation or JRA-55 and the climate value. Average zonal wind at 850hPa for the 30 months for the (c) 2015 experiment. (d) Same as (c), but for the zonal wind of the JRA-55 data; JAS.

Fig. 4 Distribution of TC genesis in the 2015 experiment. Black triangles denote the positions of TCG per the experiment and red triangles denote the observed TCG points per the IBTrACS in July 2015.

Fig. 5 Box and whisker plots of the number of TCs. From left to right; NP, WNP, and ENP in the 2015 experiment. The orange circles are the average values and the red circles are observed number of TCG points in July 2015.

Fig. 6 Time–longitude diagram of the average zonal winds (average from 0°N to 5°N) at 850 hPa over the 30 months of the 2015 experiment. The black triangles are the positions of TC genesis between from 5°N to 15°N in the experiment.

Fig. 7 Average vertical wind shear for the 30 months for the (a) 2015 experiment. (b) Same as (a), but for the 2015JAS of the JRA-55 data.

Fig. 8 Distribution of the number of TC genesis in (a) 2015 experiment. (b) Difference between PMMclm and the control experiments. (c) Difference between IOclm and the control experiments. The number of TC-genesis is counted in boxes of 5 degrees square.

Fig. 9 (a) Average SLP for the 30 months for the PMMclm experiment and difference between PMMclm and the control experiments. (b) Same as (a), but for the IOclm experiment. The areas drawn diagonal line show where the t-test is 5% significant..

Fig. 10 Average zonal winds at 850 hPa for the 30 months for (a) the PMMclm experiment and (b) the IOclm experiment. The black triangles denote the positions of TC genesis of the experiments. The black triangles are the positions of TC genesis in each experiment. (c) Difference between PMMclm and the control experiments. (d) Difference between IOclm and the control experiments.

The black triangles are the positions of TC genesis in Fig. 10a and 10b. The areas drawn diagonal line show where the t-test is 5% significant.

Fig. 11 Average vertical wind shear for the 30 months for the (a) PMMclm experiment and (b) IOclm experiment. (c) Difference between PMMclm and the control experiments. (d) Difference between IOclm and the control experiments. The areas drawn diagonal line show where the t-test is 5% significant.

Fig. 12 Differences of the wind vector (vector) at 850hPa and SST (shade) (a) between the control and PMMclm experiments, (b) between El Niño + PMM real and El Niño real experiment and (c)between PMM real and Allclm experiments. The contour shows (a) SST in PMMclm experiment, (b) SST in El Niño real experiment and (c) SST in Allclm experiment.

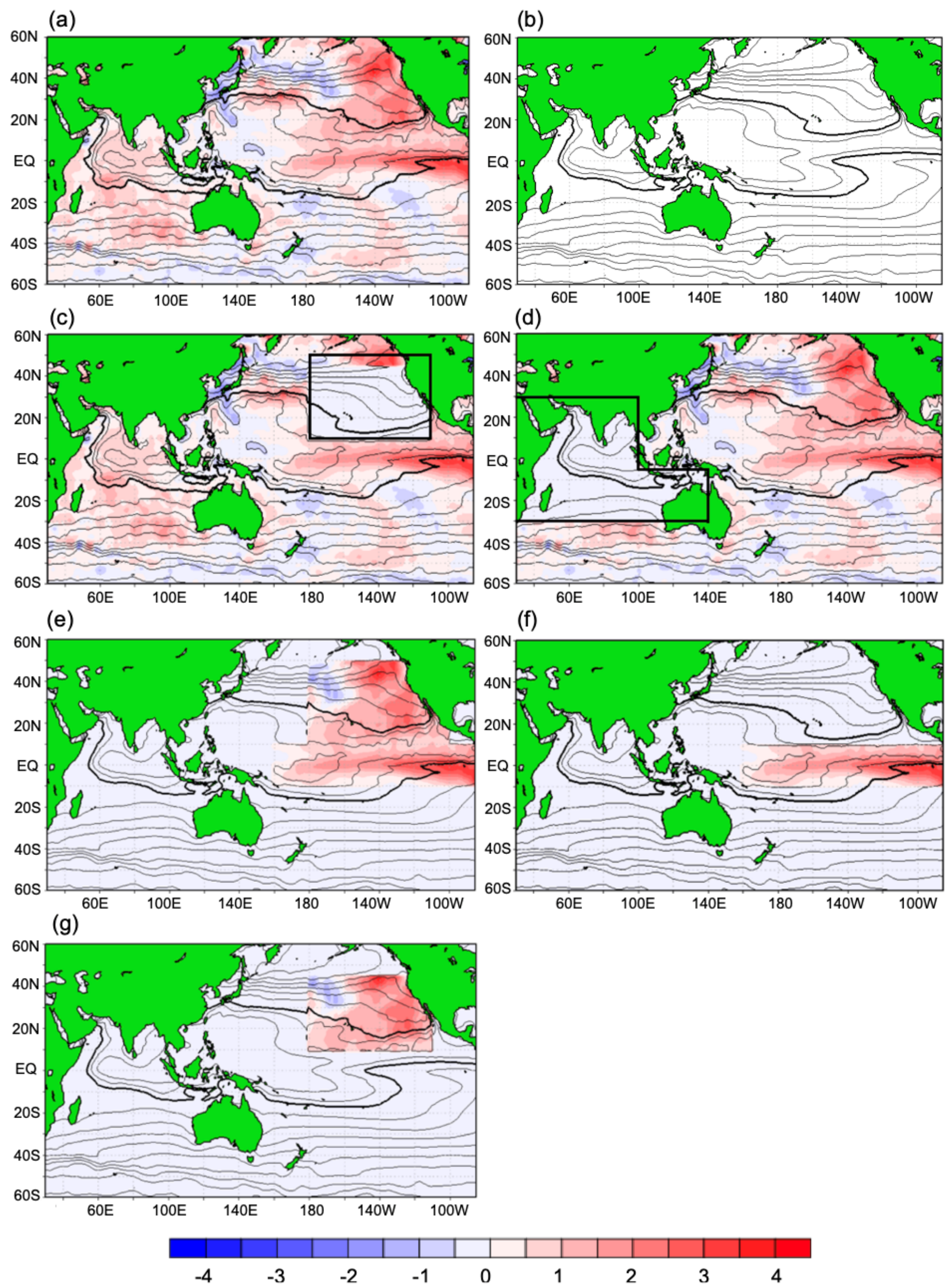


Fig. 1 SST distributions of (a) the 2015 experiment, (b) the Allclm experiment, (c) the PMMclm experiment, (d) the INDclm experiment, (e) the PMM + El Niño experiment, (f) the El Niño experiment and (g) the PMMreal experiment. Only

SSTs in the region (30°E–85°W/60°S–60°N) are shown. The contours denote the values of SST in July 2015 and the shades are the differences between experiments and the climate value (1982–2011, July average). Bold lines show that SST is 300K. Solid lines of low latitude side are drawn every 1K, while solid lines of high latitude side are drawn 3K.

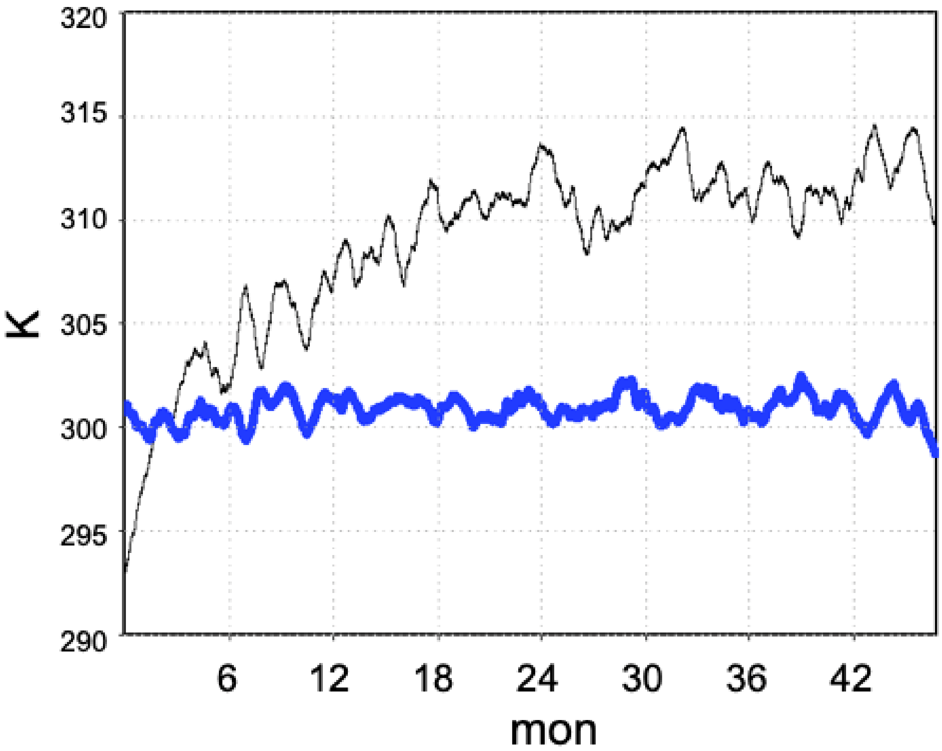


Fig. 2 Time series (moving average of anteroposterior 2 weeks) of the domain mean surface temperature for 46 months in the 2015 experiment. The black line denotes Eurasian continent (60°E–120°E/50°N–60°N), the blue line denotes Indochinese Peninsula (98°E–106°E/14°N–24°N).

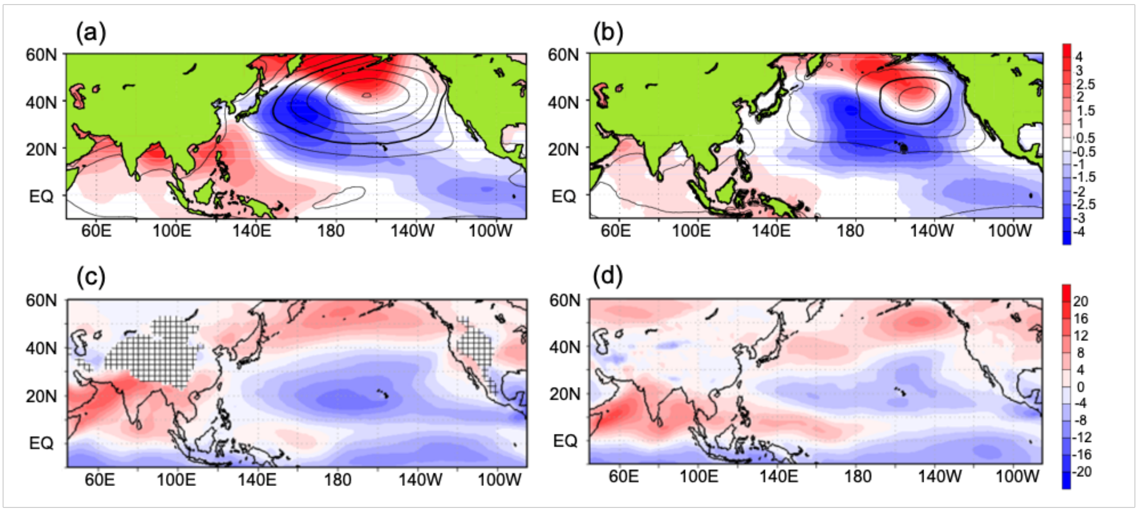


Fig. 3 Average SLPs over the 30 months of (a) the 2015 experiment. (b) Same as (a) but for the SLP of JRA-55; (b) JAS 2015. The contour in Figs. 3a and 3b denotes the each SLP, respectively. The shade denotes the difference between the value of simulation or JRA-55 and the climate value. Average zonal wind at 850hPa for the 30 months for the (c) 2015 experiment. (d) Same as (c), but for the zonal wind of the JRA-55 data; JAS.

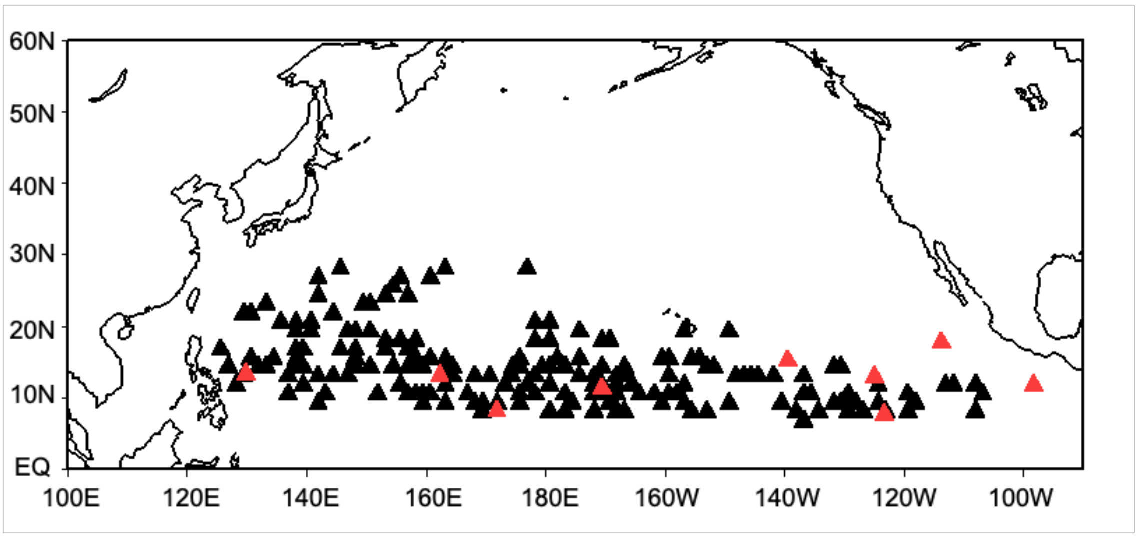


Fig. 4  Distribution of TC genesis in the 2015 experiment. Black triangles denote the positions of TCG per the experiment and red triangles denote the observed TCG points per the IBTrACS in July 2015.

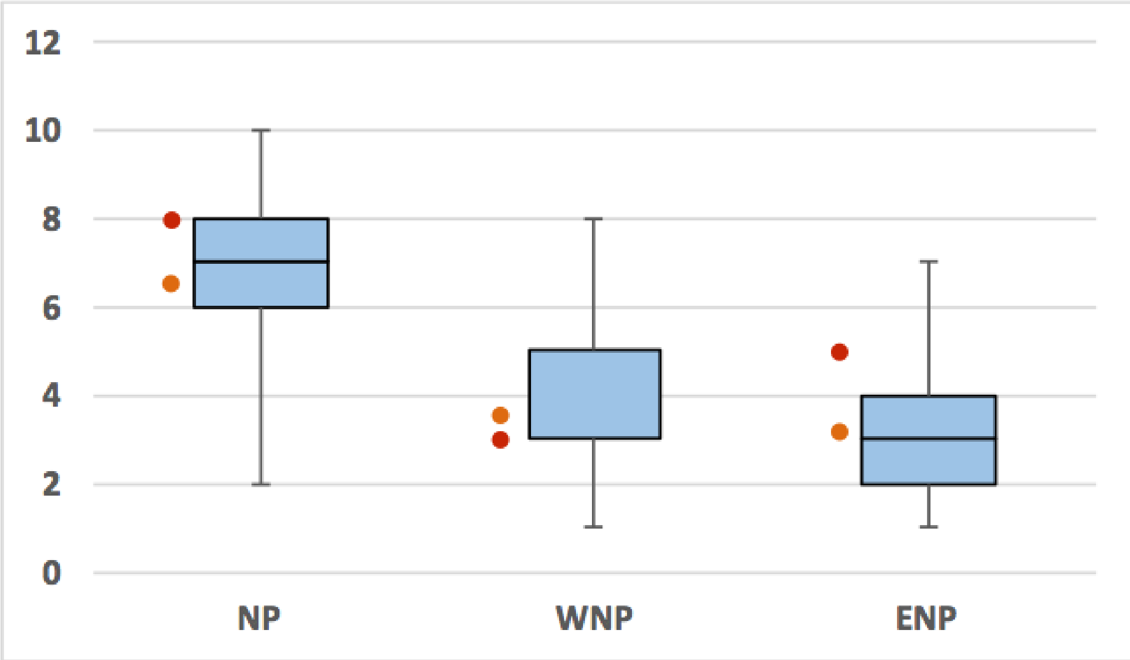


Fig. 5 Box and whisker plots of the number of TCs. From left to right; NP, WNP, and ENP in the 2015 experiment. The orange circles are the average values and the red circles are observed number of TCG points in July 2015.

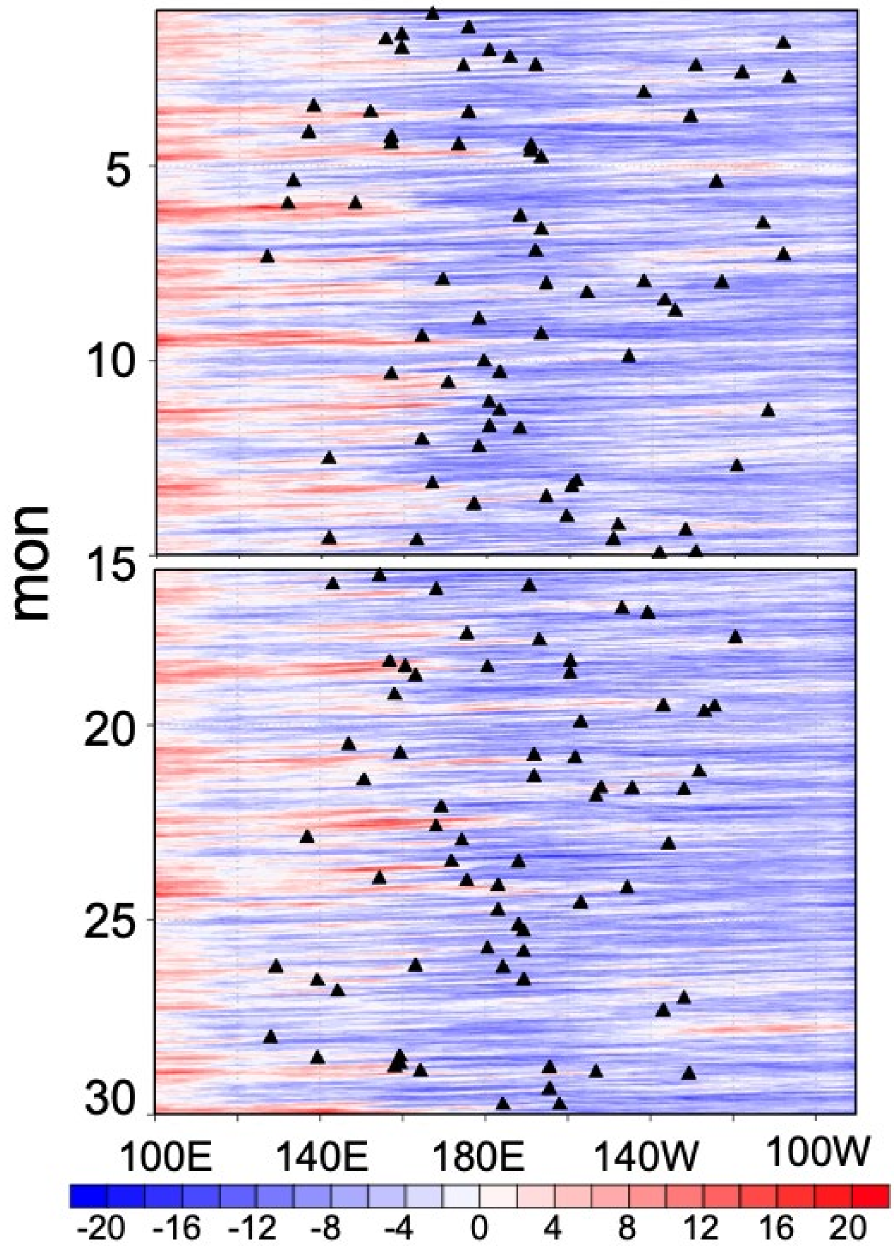


Fig. 6 Time–longitude diagram of the average zonal winds (average from 0°N to 5°N) at 850 hPa over the 30 months of the 2015 experiment. The black triangles are the positions of TC genesis between from 5°N to 15°N in the experiment.

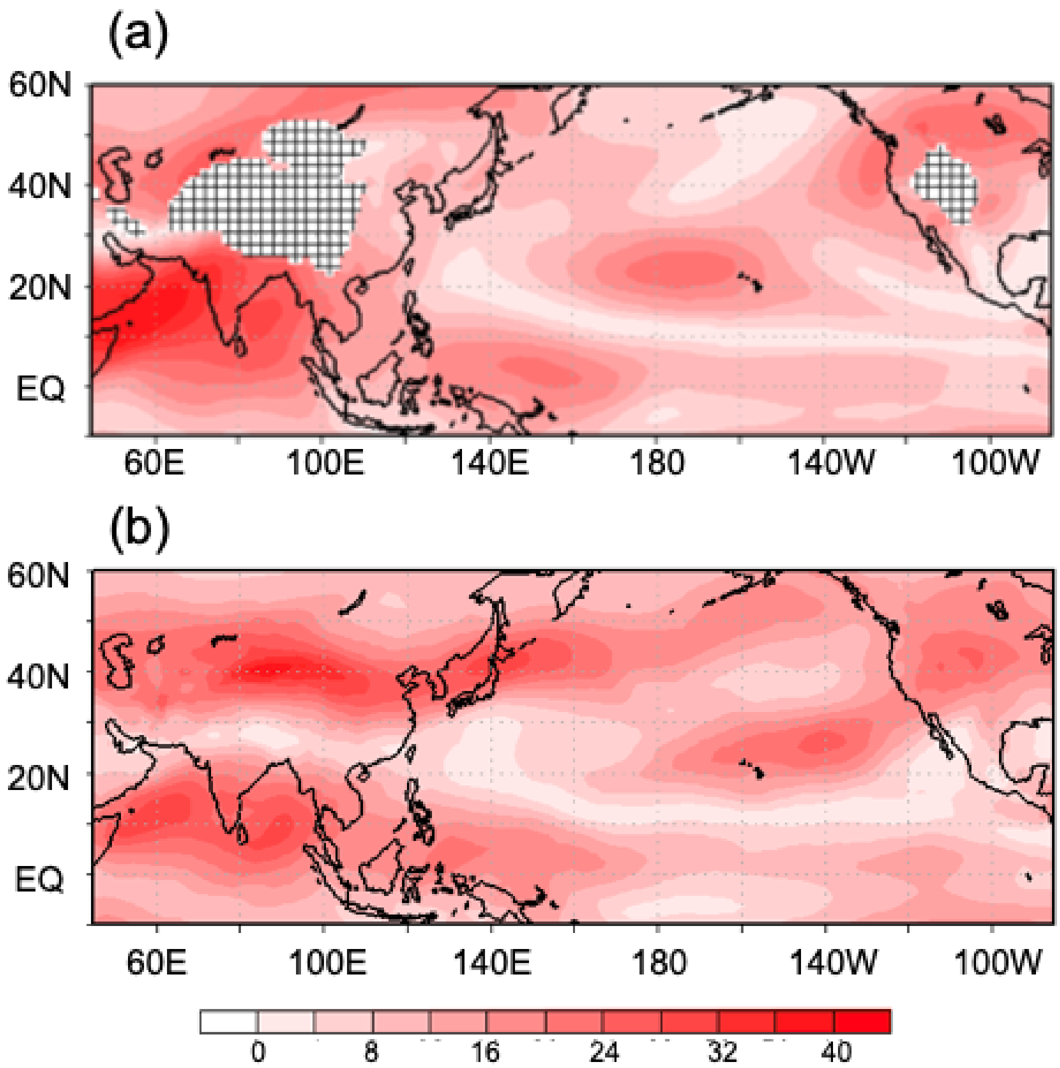


Fig. 7 Average vertical wind shear for the 30 months for the (a) 2015 experiment. (b) Same as (a), but for the 2015JAS of the JRA-55 data.

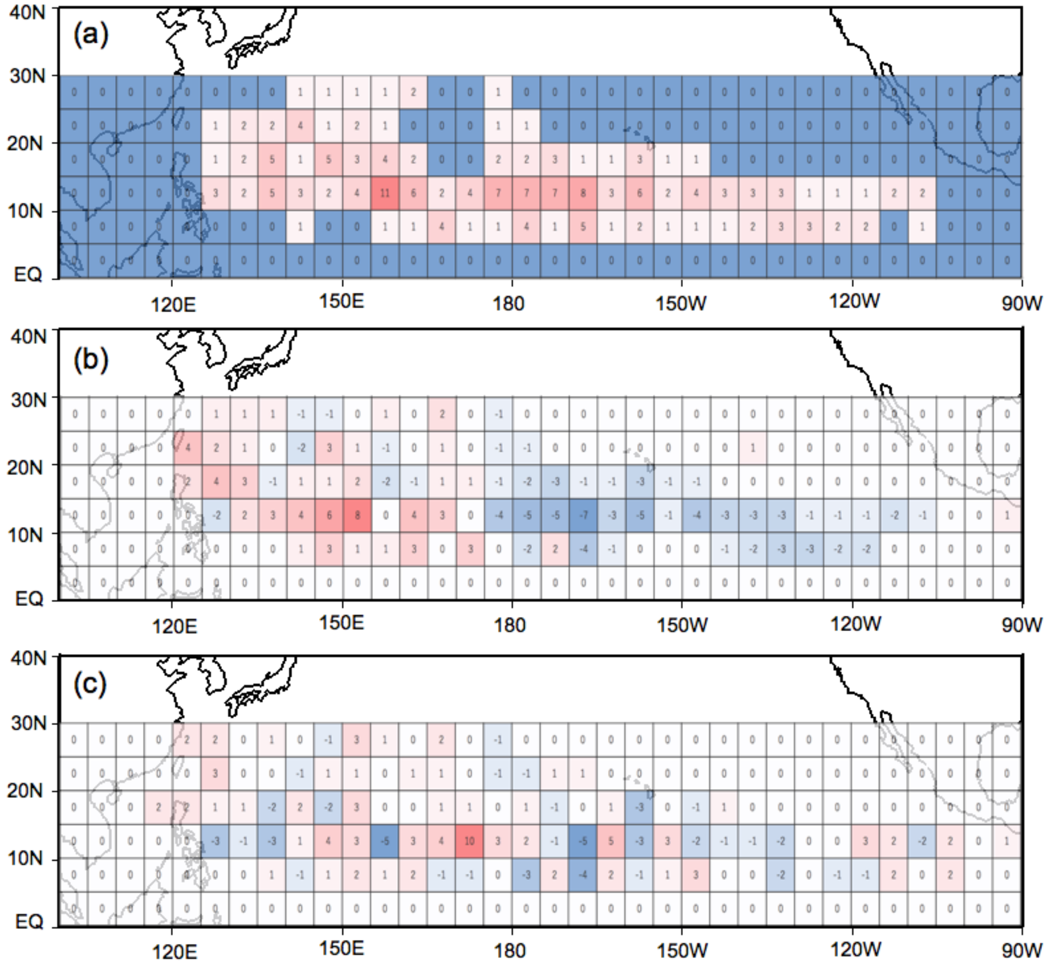


Fig. 8  Distribution of the number of TC genesis in (a) 2015 experiment. (b) Difference between PMMclm and the control experiments. (c) Difference between IOclm and the control experiments. The number of TC-genesis is counted in boxes of 5 degrees square.

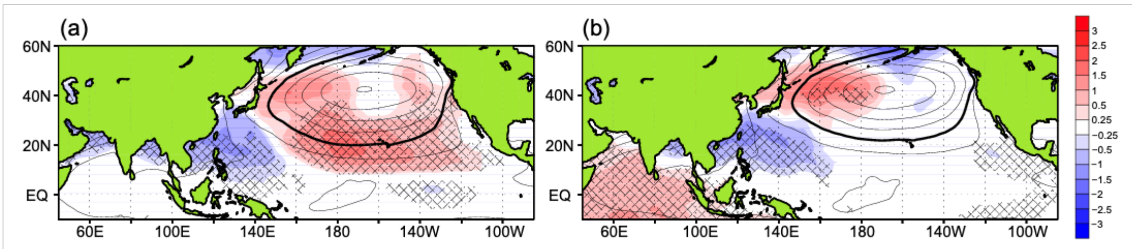


Fig. 9 (a) Average SLP for the 30 months for the PMMclm experiment and difference between PMMclm and the control experiments. (b) Same as (a), but for the IOclm experiment. The areas drawn diagonal line show where the t-test is 5% significant.

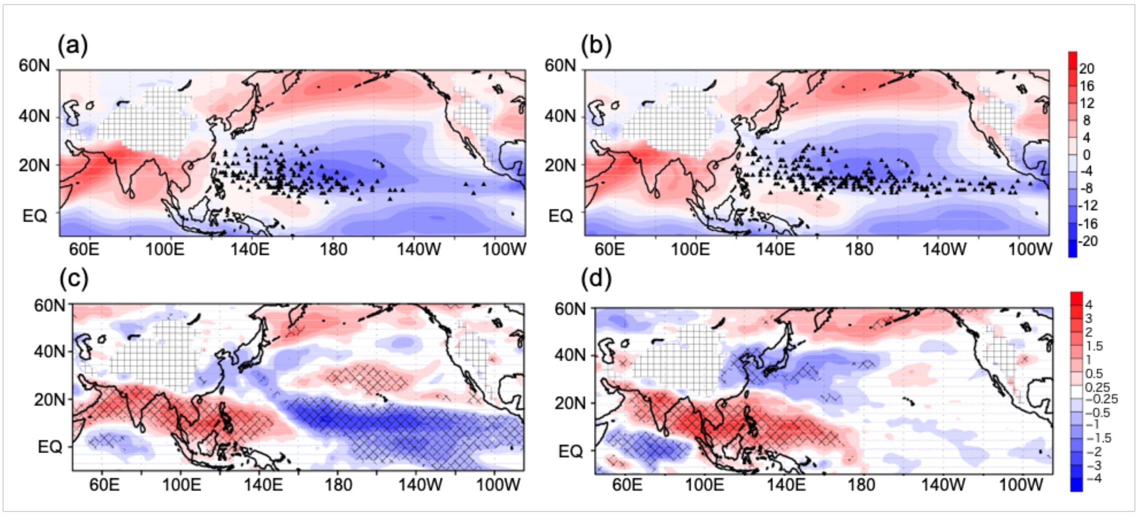


Fig. 10 Average zonal winds at 850 hPa for the 30 months for (a) the PMMclm experiment and (b) the IOclm experiment. The black triangles denote the positions of TC genesis of the experiments. The black triangles are the positions of TC genesis in each experiment. (c) Difference between PMMclm and the control experiments. (d) Difference between IOclm and the control experiments. The black triangles are the positions of TC genesis in Fig. 10a and 10b. The areas drawn diagonal line show where the t-test is 5% significant.

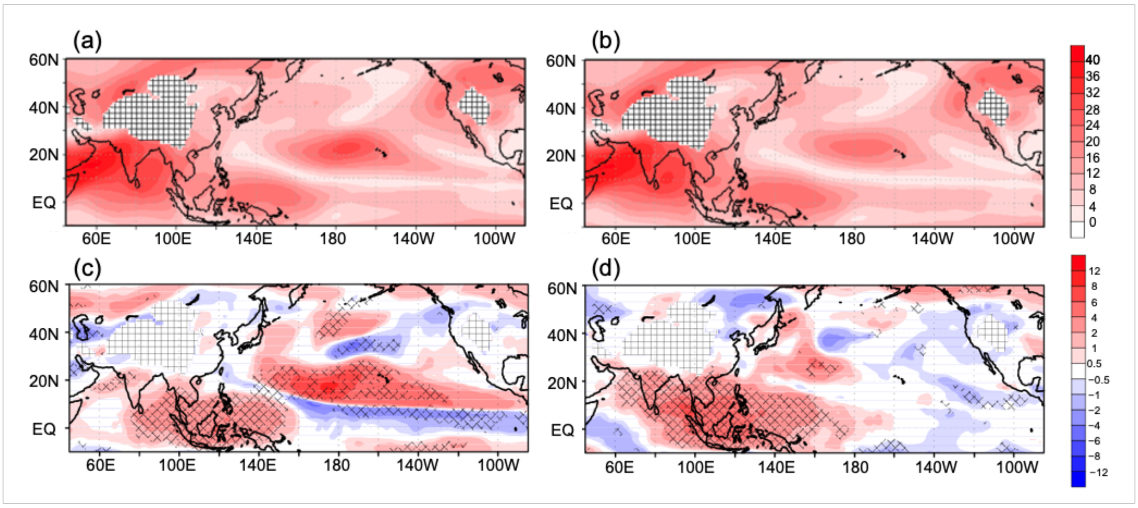


Fig. 11 Average vertical wind shear for the 30 months for the (a) PMMclm experiment and (b) IOclm experiment. (c) Difference between PMMclm and the control experiments. (d) Difference between IOclm and the control experiments. The areas drawn diagonal line show where the t-test is 5% significant.

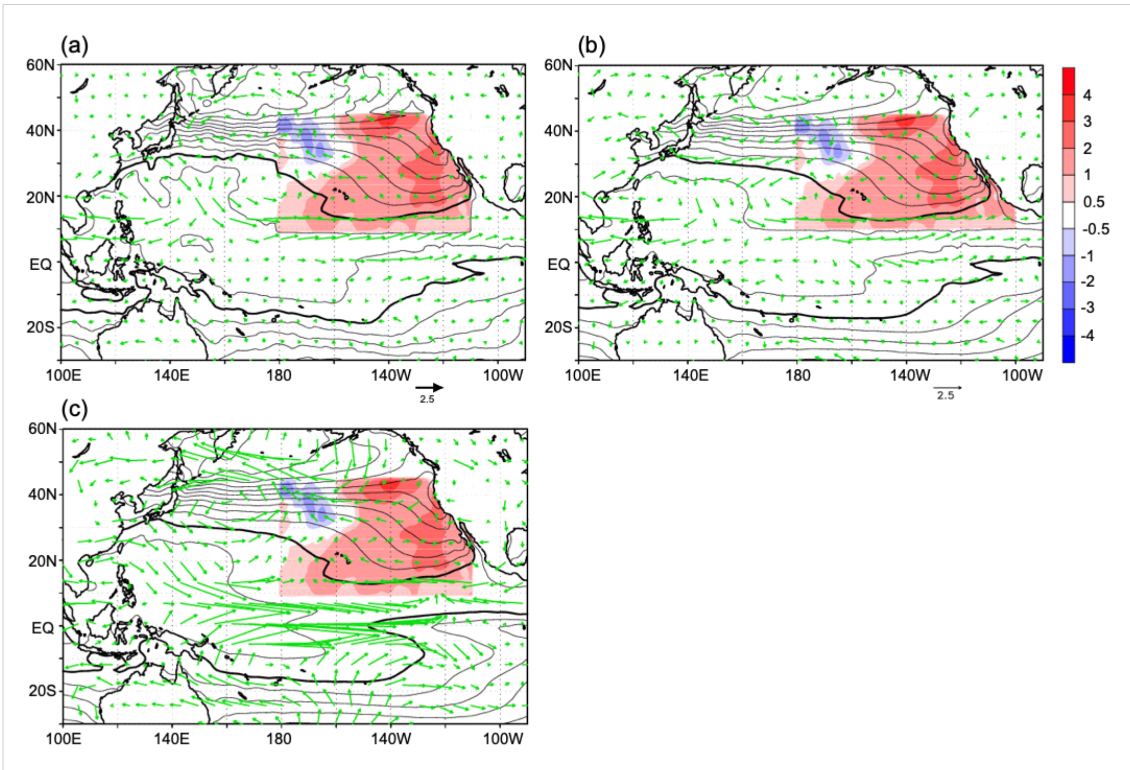


Fig. 12 Differences of the wind vector (vector) at 850hPa and SST anomaly (shade) (a) between the control and PMMclm experiments, (b) between El Niño + PMM real and El Niño real experiment and (c)between PMM real and Allclm experiments. The contour shows (a) SST in PMMclm experiment, (b) SST in El Niño real experiment and (c) SST in Allclm experiment.

List of Tables

Table1: It is a table that arranges whether each experiment is used in the value of 2015 or the climate value in each SST region. Circles mean using SST of 2015 and cross mark mean using SST of climate value.

| | El Niño region | PMM region | IO region | Other region |
|---|---|---|---|---|
| 2015 | ○ | ○ | ○ | ○ |
| Allclm | × | × | × | × |
| PMMclm | ○ | × | ○ | ○ |
| INDclm | ○ | ○ | × | ○ |
| El Niño + PMM real | ○ | ○ | × | × |
| El Niño real | ○ | × | × | × |
| PMM real | × | ○ | × | × |